ACS APPLIED MATERIALS & INTERFACES

www.acsami.org

Research Article

On-Demand Contact-Mode Switchable Cerebral Cortex Biosensors Enhanced by Magnetic Actuation

Luming Zhao, Hangyu Zhang, Changyong Wang, Jin Zhou, Meng Xiao, Jian Cheng, Jing Huang, Lingling Xu, Tianyu Gao, Zunhui Zhao, Zhou Li,* and Bo Liu*

Cite This: https://doi.org/10.1021/acsami.4c21235

Read Online

ACCESS | Metrics & More | Article Recommendations | Supporting Information

ABSTRACT: Nanomaterial-based field-effect transistors (nano-FETs) are pivotal bioelectronic devices that are employed for the detection of biomolecular signals, cellular interactions, and tissue responses within biosystems. The performance of these nano-FETs is significantly influenced by the interfacial characteristics between the metal electrodes and semiconductor nanomaterials, necessitating precise regulation. While the piezotronic effect is a commonly employed method for regulation, it faces limitations in certain application scenarios, particularly *in vivo* settings. In this study, a novel magnetically controllable piezoelectric device (MCPD) is designed by combining the principles of piezoelectric nano-FET biosensors with the flexibility of magnetic soft robots. This allows for remote, precise, and stable modulation of the metal−semiconductor interface properties of the MCPD through the magnetic field (MF)-induced piezotronic effect. Consequently, this leads to enhanced sensitivity in the detection of biomolecules such as dopamine and the recording of neural electrical impulses. The MCPD exhibits a reversible transition between a flat and a bent state upon the application of a MF of varying strengths and directions, with a response duration of only a few seconds. Furthermore, the unique structure of MCPD facilitates semi-invasive neural electrodes that can be brought into contact with the cerebral cortex only when required, thereby improving biocompatibility and reducing invasiveness. This innovation not only broadens the application scenarios for piezoelectric devices but also enables remote regulation, offering expanded utility in bioelectronic applications, such as implanted neural interface devices, and provides a potential strategy for the activation of implantable piezoelectric materials.

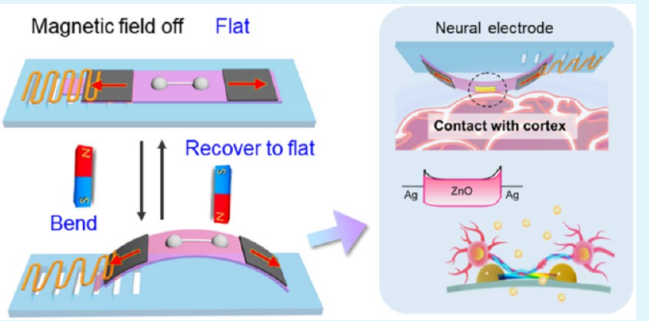

KEYWORDS: *piezotronic effect, magnetic actuation, biosensor, Schottky contact, cerebral cortex electrode*

1. INTRODUCTION

Bioelectronics, an interdisciplinary field combining biology and electronics, has seen exponential growth.[1−6] It enables signal transduction and communication between electronic components and biomolecules, cells, or tissues, with applications spanning biomolecule sensors, cardiac pacemakers, and neural interface devices.[7−11] Advancing nanotechnology has facilitated the fabrication of diverse nanomaterial-based bioelectronic devices (nanobioelectronic devices), which demonstrate significant improvements in sensitivity and biocompatibility.[12−16] These advancements are attributed to their unprecedented excellent properties compared to their bulk counterparts, including the resolution of size mismatch issues.

Notably, the nanomaterial-based field-effect transistor (nano-FET) is a fundamental platform employed in biomolecule sensing and as a microelectrode for the stimulation or recording of physiological signals.[12,17−19] However, the sensitivity of nano-FETs is often influenced by the metal electrode−semiconductor nanomaterial (M−S) interface properties and the quality of bioelectronics interfaces.[19−22] Specifically, Schottky-contact nano-FETs have shown superior sensitivity to UV, gas, and biomolecules compared to their ohmic-contact counterparts.[20,23−25] For Schottky-contact nano-FETs, the rational modulation of the M−S interface properties reflected by the Schottky barrier height (SBH) is crucial for the high-sensitivity detection of biomolecules and electrophysiological signals.[26] Prior research indicates that SBH can be reversibly modulated by various means, including ultraviolet (UV) illumination,[27] high-voltage electric fields,[28] piezotronic effects,[29,30] and triboelectric nanogenerator (TENG) treatment.[26,31] However, UV illumination is limited by the application scenario, high-voltage electric fields pose safety risks, and SBH reduction *via* TENG treatment is temporary.[26,31,32] The piezotronic effect, by contrast, offers an effective, safe, popular, and stable method for SBH modulation,

Received: December 3, 2024
Revised: March 8, 2025
Accepted: March 14, 2025

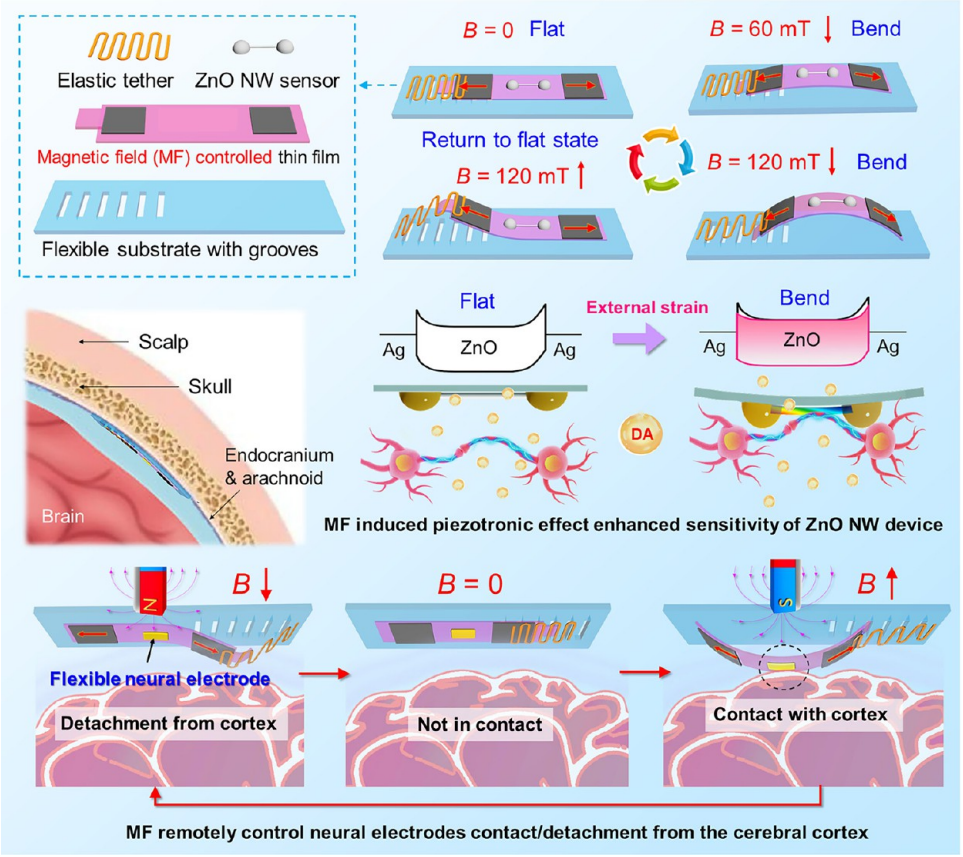

Figure 1. Conception diagram of magnetically controllable piezoelectric nano-FET/neural electrodes. The piezotronic effect can be realized by MF, and the sensitivity of piezoelectric ZnO NMW-FET biosensors for detecting dopamine and neural electric signals can be significantly enhanced. The neural electrode for contact/detachment from the cerebral cortex can also be remotely actuated by an MF.

thereby enhancing the sensitivity of piezotronic devices for detecting chemical, physical, and biological signals.[33−36]

The piezotronic effect necessitates strain or deformation in the piezoelectric nanomaterial of nano-FETs.[35,37] Typically, precise and stable external strain is applied *via* multiaxis displacement devices, which are impractical for *in vivo* implants, particularly intracranial nano-FETs. To expand the application scenarios and enhance the sensing performance of piezoelectric nano-FETs, remotely imposing precise and stable external strain/deformation is essential. Researchers have explored various remote actuation methods including optical,[38] electrical,[39] thermal,[40] and magnetic actuation.[41,42] Among these, magnetic actuation stands out for its efficiency and controllability, and unique advantages in deep tissue penetration and biocompatibility, as magnetic fields (MF) are not attenuated or distorted by biological media.[43] In recent decades, a multitude of magnetic soft robots have been developed for *in vivo* navigation in imaging, diagnosis, and therapeutic applications.[44−46]

Inspired by Coles et al.'s work on a shape-shifting electrocorticography device,[47] the MF-controlled deformation of nano-FETs presents a novel strategy to enhance the neural interface quality with brain tissue, facilitating high-quality neuroelectric signal recordings.[19,48] While studies on magnetically controllable neural microelectrodes exist, maintaining a stable biointerface between microelectrodes and tissue requires a constant MF. This study introduces a magnetically controllable piezoelectric device (MCPD) that integrates piezoelectric nano-FETs with concepts derived from magnetic soft robots (Figure 1). The MCPD can transition from a flat to a bent state with different degrees by applying MF of varying strengths and directions for seconds, in contrast to devices requiring constant MF for stability.[43,49,50] The SBHs at the Ag−ZnO interfaces of ZnO nano/microwire (NMW)-based FET are successfully regulated by piezotronic effect-induced MF-actuated deformation, enhancing the sensitivity for dopamine (DA) and neural electrical signal detection, which is crucial for the study of brain function and the diagnosis of brain diseases. Besides, flexible neural electrodes fabricated on a magnetically controllable structure realized remote control of contact or detachment from the cerebral cortex by MF actuation. This work provides a feasible strategy for the remote magnetic actuation of piezoelectric devices, improving the sensitivity and biocompatibility of implanted bioelectronic neural devices, and holds great potential for *in vivo* diagnostic and therapeutic applications.

2. RESULTS AND DISCUSSION

2.1. Fabrication of Magnetically Driven Film (MDF).

The fabrication of magnetically driven substrate films is the basis for developing piezoelectric nano-FET/neural electrodes that can be remotely actuated by MF. Drawing on many published works related to magnetic soft robots,[41,44] in this work, a magnetically driven film (MDF) was prepared by mixing NdFeB particles (400 #) and PDMS (SYLGARD 184) solution and magnetizing the obtained magnetic composite film (0.2 mm) by applying a strong uniform B field (1.0 T). The schematic diagram and photograph of the magnetization

https://doi.org/10.1021/acsami.4c21235
ACS Appl. Mater. Interfaces XXXX, XXX, XXX−XXX

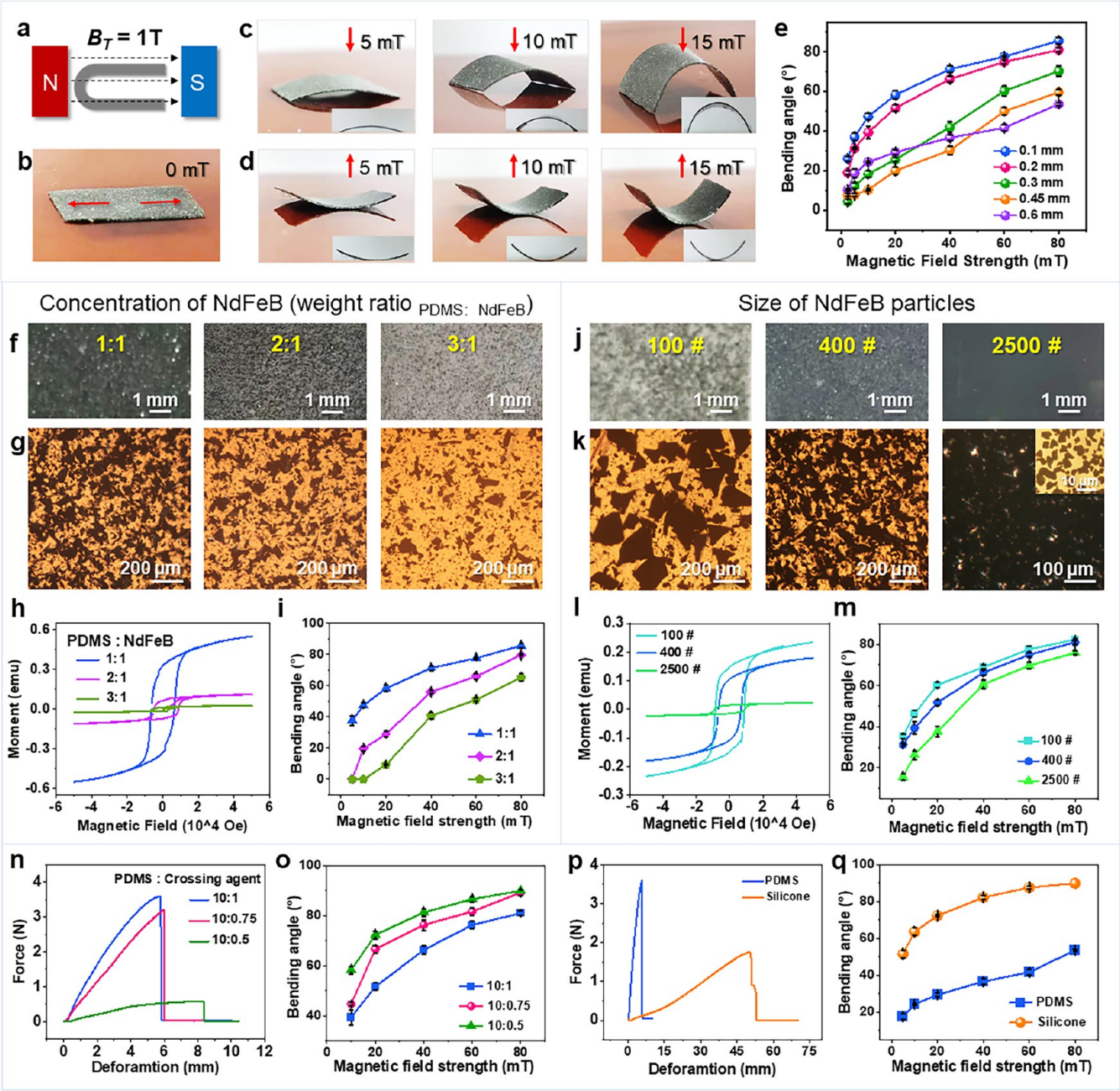

Figure 2. Fabrication and properties of the magnetically driven film (MDF). (a) Magnetization profile of MDF. (b–d) Photograph of the MDF under magnetic actuation. (e) Bending angles of MDFs with different thicknesses. (f, g) Photographs and optical microscopy images of MDFs with different concentrations of NdFeB particles. (h), (i) Magnetization versus magnetic field (M–H) loop and bending angle of MDFs containing different concentrations of NdFeB particles. (j, k) Photographs and optical microscopy images of MDFs with different sizes of NdFeB particles. (l, m) M–H loop and bending angle of MDFs with different sizes of NdFeB particles. (n, o) Stress–strain curve and bending angle of MDFs with different ratios of PDMS and crossing agent. (p, q) Stress–strain curve and bending angle of MDFs made of PDMS (SYLGARD 184) and silicone (Ecoflex 00–10). Error bars in e, i, m, o, and q indicate SD for n = 3 measurements.

process are shown in Figures 2a and S1, respectively. The distributed magnetizations of the MDF without MF are shown in Figure 2b; the magnetization directions of the left and right ends are opposite. When the MF with the direction perpendicular to the flat surface is applied, the MDF bends upward or downward depending on the direction of the MF, and the bending angle increases with the increase of MF strength (Figure 2c,d). The MF strength can be changed by controlling the distance between the MDF and the magnet (Figure S2).

The effect of thickness on the bending angle is studied, and the curves in Figure 2e show that the bending angle of the MDF under the same MF strength roughly decreases with the thickness of the MDF. This can be attributed to the thinner MDF being more flexible and lighter and easier to bend under the same MF strength. When the MF strength is lower than 20 mT, the bending angle of the MDF corresponding to 0.6 mm is larger than that corresponding to 0.3 mm and 0.45 mm because the magnetic force is higher than the gravity force under this condition. To further confirm this claim, a low MF

https://doi.org/10.1021/acsami.4c21235
ACS Appl. Mater. Interfaces XXXX, XXX, XXX–XXX

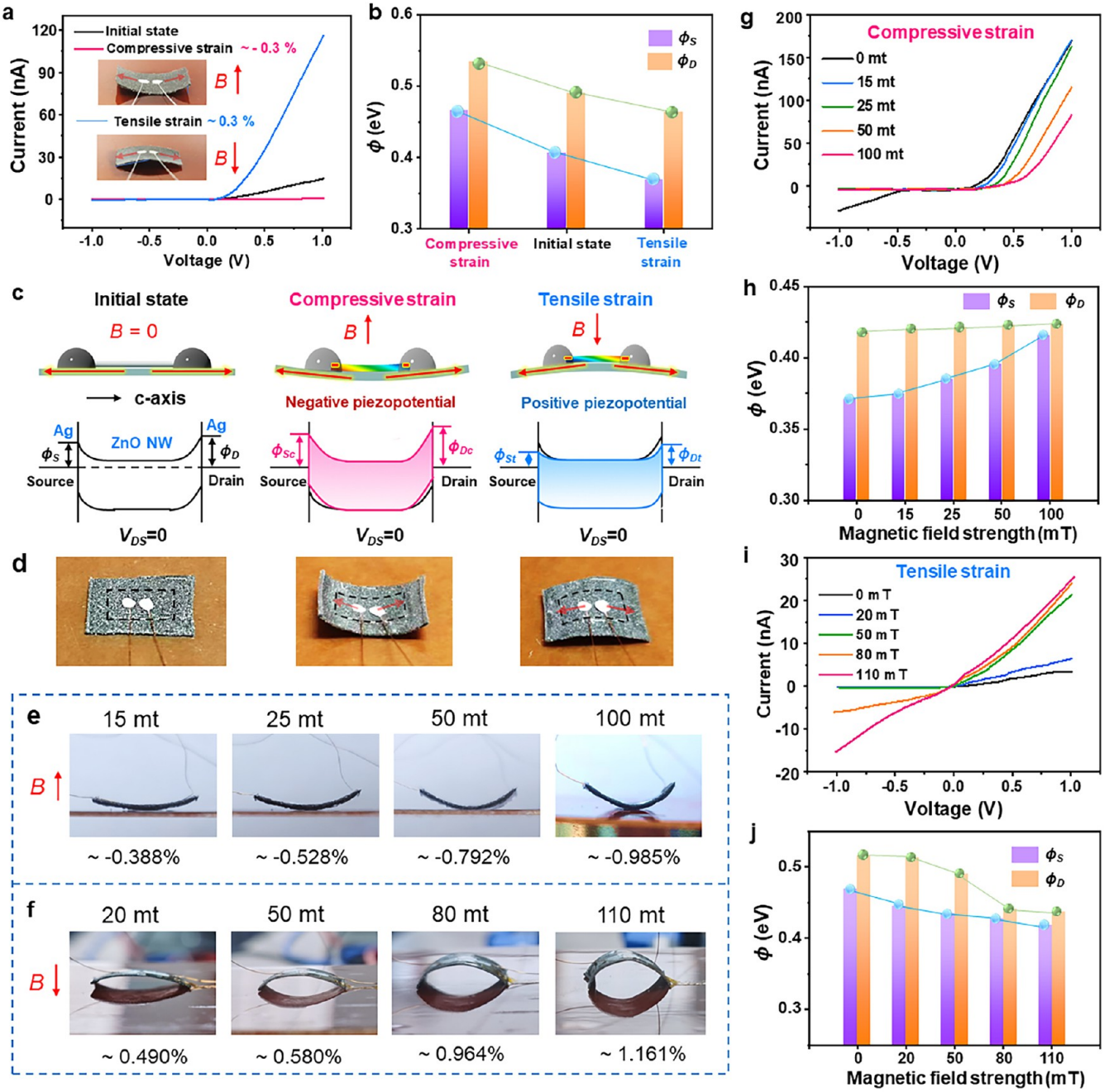

Figure 3. Magnetic actuation of the piezotronic effect. (a, b) *I*−*V* curves and SBH of the ZnO NMW-based device fabricated directly on MDFs in different directions of MF. (c) Energy band diagrams of the fabricated ZnO NMW-based device in different directions of MF. (d−f) Photograph of the ZnO NMW-based device fabricated on a thin Kapton film attached to MDFs in different directions and strengths of MF. (g, h) *I*−*V* curves and SBH of the fabricated ZnO NMW-based device under MF-induced compressive strain. (i, j) *I*−*V* curves and SBH of the fabricated ZnO NMW-based device under MF-induced tensile strain.

strength of 5 mT in the direction opposite to gravity was applied, as shown in Figure S3; the MDF with a thickness of 0.6 mm has a stronger ability to overcome gravity than that of 0.3 mm, which further demonstrates the phenomenon shown in Figure 2e.

The effects of the concentration and size of the NdFeB particles on the magnetic properties of the MDF are investigated. Photographs and optical microscopy images of the MDF with PDMS and NdFeB mixing mass ratios of 1:1, 2:1, and 3:1 are shown in Figure 2f,g. The magnetic responses of the MDF containing different concentrations of NdFeB particles are measured by the physical property measurement system, and it can be seen that with an increase of the NdFeB concentration, the residual magnetization strength increases (Figure 2h) and the bending angle of the MDF with the same MF strength also increases with the concentration of NdFeB particles (Figure 2i). The results indicate that a higher NdFeB content makes the MDF more sensitive to MF. Photographs and optical microscopy images of MDF consisting of NdFeB particles of grit sizes 100, 400, and 2500# are shown in Figure 2j,k, where the particle sizes corresponding to 100, 400, and 2500# are 200 μm, 50, and 5 μm, respectively. The M−H loop

https://doi.org/10.1021/acsami.4c21235
ACS Appl. Mater. Interfaces XXXX, XXX, XXX−XXX

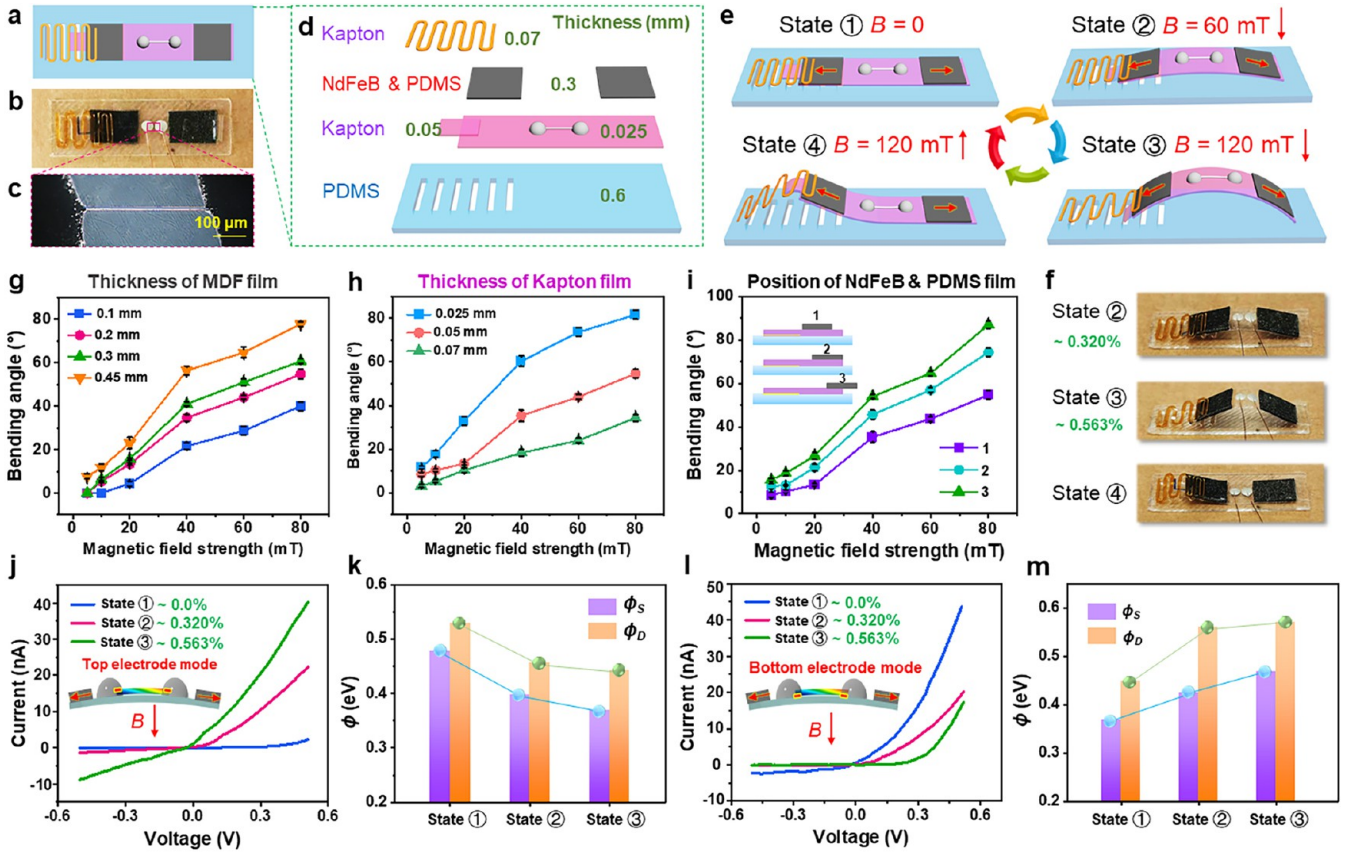

Figure 4. Fabrication of the magnetically controllable piezoelectric device (MCPD). (a, b) Plane schematic diagram and photograph of the MCPD. (c) Optical microscopy image of the ZnO NMW-based device. (d) Hierarchical structure diagram of the MCPD. (e, f) Deformation process diagram and photograph of the MCPD in different states (① flat, ② slight bend, ③ obvious bend, and ④ recover). (g–i) Bending angles of the magnetically controllable substrate of the piezoelectric biosensor with different thicknesses of MDFs, different thicknesses of the Kapton films, and different positions of the MDF on the Kapton film. Error bars in g, h, and i indicate the SD for $n = 3$ measurements. (j, k) I–V curves and SBH of the ZnO NMW-based piezoelectric biosensor in the top electrode mode under MF-induced tensile strain. (l, m) I–V curves and SBH of the ZnO NMW-based piezoelectric biosensor in the bottom electrode mode under MF-induced tensile strain.

of the MDF with different sizes of NdFeB particles is shown in Figure 2l. With an increase of the NdFeB particle size, the residual magnetization strength increases, and the bending angle of the MDF under the same MF strength also increases with the size of the NdFeB particles (Figure 2m). These results indicate that NdFeB particles with larger sizes make the fabricated MDF more sensitive to MF.

Finally, the effect of the mechanical properties of the elastomers on the magnetic properties of the MDF is studied. The mechanical properties of the PDMS (SYLGARD 184) elastomer can be modulated by changing the mass ratio of the PDMS solution and the crossing agent. The reduction in the content of the cross-linker makes the PDMS elastomer more flexible and easier to deform (Figure 2n), and the bending angle of the MDF and its sensitivity to MF can be improved by enhancing the flexibility of the PDMS elastomer (Figure 2o). Moreover, the magnetic responses of the MDF can be further enhanced by replacing the PDMS elastomer with a highly elastic silicone rubber (Ecoflex 00–10) (Figure 2p,q).

2.2. Magnetic Actuation of the Piezotronic Effect. To study the magnetic actuation of the piezotronic effect, a ZnO NMW-based FET device was fabricated on a flexible substrate made of MDF. It can be observed from the I–V curves in Figure 3a that the output current of the ZnO NMW-based FET device in the range of 0 V − 1.0 V decreased by the MF (5 mT)-induced compressive strain and increased by the tensile strain-induced MF (5 mT) in the opposite direction. The SBHs of the source and drain calculated from Figure 3a increase and decrease with compressive strain and tensile strain, respectively (Figure 3b). Figure 3c exhibits the energy band change of the ZnO NMW-based device under compressive strain and tensile strain induced by MF in opposite directions. ZnO is a typical piezoelectric material and by applying external strain on it, an internal piezoelectric potential (piezopotential) can be produced inside the material. The generated piezopotential can serve as a gate voltage that modulates the carrier flow through a ZnO NMW-based FET.[51,52] Compared with traditional gate-controlled nano-FETs, the gate electrode is absent and the gate voltage is replaced by the piezopotential. The fabricated ZnO NMW-based device is the top electrode configuration, and the electrical contact areas formed between Ag electrodes and the two ends of the ZnO NMW are marked with red dots.[53] When the compressive strain and tensile strain are applied to the device, the induced piezopotential formed at the electrical contact areas are negative and positive, which increase and decrease the SBHs at both ends, respectively. However, when the MF strength reaches 10 mT, the Ag electrodes are detached from the MDF substrate because it is challenging to deposit metals and media on PDMS in general.[54]

For secure fixation of the Ag electrodes on the MDF substrate, the ZnO NMW-based device is prepared on a thin

https://doi.org/10.1021/acsami.4c21235
ACS Appl. Mater. Interfaces XXXX, XXX, XXX–XXX

Kapton film (0.025 mm), which is fixed on the MDF substrate made of PDMS because silicone rubber is too soft to apply deformation to the Kapton film. Photographs of the as-fabricated ZnO NMW-based device in different directions and strengths of MF are shown in Figure 3d−f. The degree of compressive strain and tensile strain increase with the strength of MF, which leads to the downward and upward shifts of the $I-V$ curves (Figure 3g,i), and the increase and decrease of SBH at the source and drain (Figure 3h,j), respectively. In this section, it is demonstrated that the MF-induced deformation of the substrate effectively induced the piezotronic effect and realized SBH modulation of a piezoelectric device.

2.3. Fabrication of the Magnetically Controllable Piezoelectric Device (MCPD). Although the piezotronic effect realized by MF-induced external strain has been demonstrated, the stabilizing effect of the piezotronic effect on piezoelectric devices cannot be realized without maintaining the stability of the direction and strength of the MF. Once the MF is removed or changed, the piezoelectric deformation is immediately withdrawn or changed accordingly. However, excessive strength of MF or prolonged action may harm the human body. To realize a stable piezoelectric deformation that can be maintained without long-term loading of an MF with high strength, a novel structure, illustrated in Figure 4, was proposed.

A plane schematic diagram and photograph of the magnetically controllable piezoelectric device (MCPD) are shown in Figure 4a,b. The piezoelectric device is a typical ZnO NMW-based device whose optical microscopy image is shown in Figure 4c, and the diameter of the ZnO NMW is about 6 μm. The hierarchical structure diagram of the MCPD is shown in Figure 4d, where it is assembled with a layer of PDMS substrate (0.6 mm) with several rectangular grooves, a ZnO NMW-based FET device fabricated on a flexible layer of the Kapton film (0.025 mm), a patch of the Kapton film (0.5 mm) that can be inserted into the rectangular groove and thus immobilized for MF-driven external strain, 2 pieces of MDF, and an elastic tether made of the Kapton film (0.5 mm) in the S pattern.

The magnetic driving mode and the process of MCPD in different states are illustrated in Figure 4e. In the initial state (i.e., state ①), the MCPD is in the flat mode with no external strain applied to the piezoelectric device without MF. When the MF in the direction perpendicular to the flat surface increased, the Kapton substrate of the piezoelectric device was bent by the MDF. With an increase of MF strength, the patch was inserted into the groove of the PDMS substrate at 60 mT. Under these conditions, the piezoelectric device was slightly bent (i.e., state ②). It is worth noting that state ② can be maintained after the MF is withdrawn. By contrast, when the MF is low, although the MCPD deforms when MF is applied, this deformation is not enough to embed the MCPD patch into the groove of the PDMS substrate, so the MCPD no longer remains in the bent state after the MF is withdrawn. When the MF strength reached 120 mT, the piezoelectric device was further bent because the patch moved and was inserted into the adjacent right groove; the MCPD was in state ③. When the external strain applied to the piezoelectric device needs to be withdrawn and returned the device to state ①, the MF with a reversed direction of 120 mT can be applied to the MCPD in state ③, the piezoelectric device can be bent in the opposite direction causing the patch to pull away from the groove (state ④), and the device is restored to state ① under the traction of the elastic tether after the MF disappears. The photographs of MCPD at different states are shown in Figure 4b (state ①) and Figure 4f (states ②−④), and the video of the MCPD deformation process is shown in Movie 1, where the state transition can be realized by applying MF of different directions or strengths with a duration of only a few seconds. It can be seen from Movie 1 that, besides the strength of MF, the change in the MF direction can also contribute to the state transition of MCPD; for instance, the shift of the magnet to the right promotes the transition from state ② to state ③, and the shift of the magnet to the right promotes the transition from state ③ to state ④. Therefore, the direction and strength of the MF should be combined to realize the magnetic actuation of the MCPD.

During the process of structural optimization of MCPD, the influence of the thickness of MDF, the Kapton film substrate, and the position of MDF on the Kapton film substrate on the bending angle of the Kapton film driven by MF with different strengths is studied. The schematic diagram of the experimental setup is shown in Figure S4. Under the same MF strength, the increase of the MDF thickness improves the bending degree of the Kapton film (Figure 4g), while increasing the thickness of the Kapton film lowers its bending angle (Figure 4h). Besides, it can be seen from Figure 4i that the greater the distance between the fixation site of MDF and the center of the Kapton film, the greater the bending angle of the Kapton film. Based on the above results, a 0.3 mm-thick MDF and a 0.025 mm-thick Kapton film substrate are chosen to fabricate the MCPD, considering that the 0.025 mm-thick Kapton film is too soft to fix in the groove after the MF disappeared. The 0.05 mm-thick Kapton film is employed to serve as the patch of the MCPD. Although highly elastic silicone rubber (Ecoflex 00−10) is more responsive to magnetic fields than PDMS, it is not favorable for the elastic tether to be fixed on top of the MCPD made of silicone rubber (Ecoflex 00−10). Meanwhile, to ensure the stability and robustness of the device, PDMS is chosen to fabricate the MCPD device in this work.

The structure of MCPD can only exert tensile strain on the piezoelectric device. For the ZnO NMW-based device with the top electrode configuration, the induced piezopotential at the M−S interfaces (red regions in the inset of Figure 4j) is positive with the tensile strain applied by MCPD, the current in the range of −0.5 to 0.5 V increases (Figure 4j), and the calculated SBHs at the source and drain decrease with the state variation of the device (states ①→②→③) (Figure 4k). Whereas, for the ZnO NMW-based device with the bottom electrode configuration, the induced piezopotential at the M−S interfaces (red regions in the inset of Figure 4l) is negative with the tensile strain, and the variation tendency of the $I-V$ curves and SBHs during the same process of state switching are reversed (Figure 4l,m). The results in Figure 4j−m are consistent with the tendencies in the previous work.[53] Moreover, the repeatability and stability of MCPD were investigated. As shown in Figures S5 and S6, the variation in the $I-V$ curves and SBHs exhibits the same trend during 3 repetitions, and the $I-V$ curve and SBHs hardly changed under stable piezoelectric deformation. For piezoelectric devices, the novel structure of MCPD successfully achieved stable modulation of SBHs through short-term MF loading.

2.4. Piezotronic Effect Enhanced Sensing Performance of ZnO NMW-Based Biosensor. Detection of neurotransmitters and neural electrical signals in situ is of

https://doi.org/10.1021/acsami.4c21235
ACS Appl. Mater. Interfaces XXXX, XXX, XXX−XXX

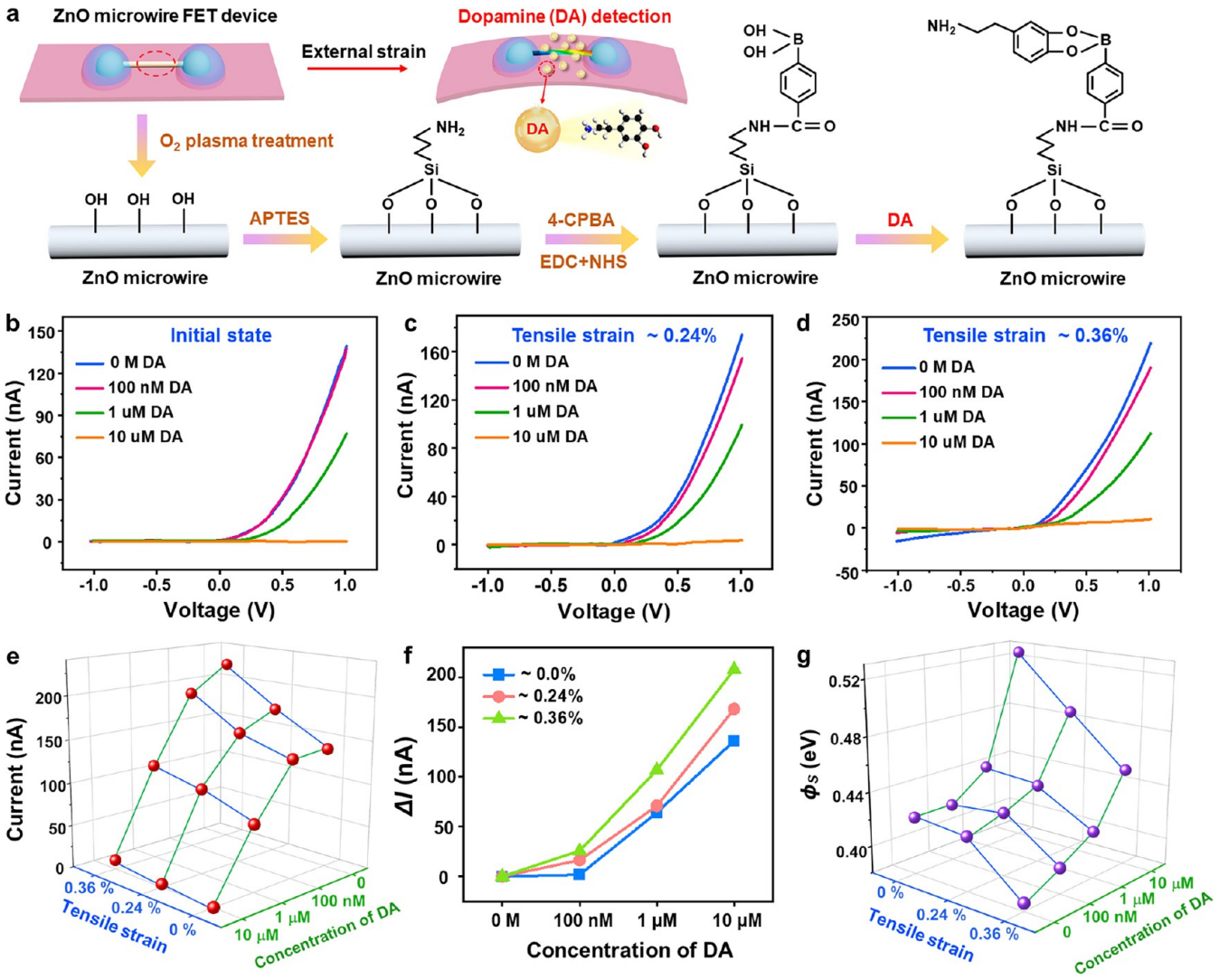

Figure 5. Piezotronic effect enhanced the performance of the ZnO NMW dopamine sensor. (a) Surface functionalization of the ZnO NMW FET device for DA detection. (b) $I-V$ curves of the ZnO NMW DA sensor at different DA concentrations; no external strain was applied. (c, d) $I-V$ curves of the ZnO NMW DA sensor at different DA concentrations under tensile strains of 0.24 and 0.36%. (e) 3D graph showing the current response of the ZnO NMW DA sensor under different strains and DA concentrations. (f) Absolute current response of the ZnO NMW DA sensor at different DA concentrations, with tensile strains ranging from 0 to 0.36%. (g) 3D graph showing SBH of the ZnO NMW DA sensor under different strains and DA concentrations.

great significance for decoding brain function and exploring therapeutic methods for brain diseases. DA is an important neurotransmitter in the human body and plays a key regulatory role in the central nervous system. For patients with Parkinson's disease, the DA levels in the cerebrospinal fluid are significantly lower than those in healthy people; therefore, DA is a frequently used cerebrospinal fluid biomarker for diagnosing Parkinson's disease.[55] To achieve rapid, low-cost, and precise detection of DA levels, many kinds of FET-based DA biosensors have been proposed. Utilizing surface functionalization methods serviced from these works,[56,57] the fabricated ZnO NMW FET device was functionalized to exhibit sensitivity and selectivity to DA molecules (Figure 5a). First, the ZnO NMW FET device was subjected to O_2 plasma treatment to introduce −OH groups on the ZnO NMW surface. Then, the amine groups were formed by soaking them in 3-aminopropyltriethoxysilane (APTES). The obtained amine groups were coupled to carboxyphenyl boronic acid (CPBA) under the activation of *N*-hydroxy succinimide (NHS) and *N*-ethyl-*N*′-(3-(dimethylamino)propyl) carbodiimide (EDC). Therefore, the specific binding of DA and CPBA formed a negatively charged DA-boronate ester on the ZnO NMW surface, which affected the SBH at the Ag−ZnO interface and channel conductivity and changed the $I-V$ curve of the ZnO NMW FET device. After surface modification, the lowest DA concentration detected by the ZnO NMW sensor was 500 nM (Figure S7). Compared with that of the unmodified ZnO NMW sensor in our previous work (500 μM),[26] the detection limit can be increased by 1000 times after surface functionalization treatment.

Previous studies have demonstrated that the piezotronic effect can be used to remarkably enhance the performance of Schottky-contacted ZnO NMW biosensors. Hence, in this section, we study the effect of external strain induced by MF on the DA sensing properties of the Schottky-contacted ZnO NMW FET device. Figure 5b−d exhibits the performance of the DA biosensor under 0.00, 0.24, and 0.36% tensile strains, respectively, with DA concentrations ranging from 0 M to 10

https://doi.org/10.1021/acsami.4c21235
ACS Appl. Mater. Interfaces XXXX, XXX, XXX−XXX

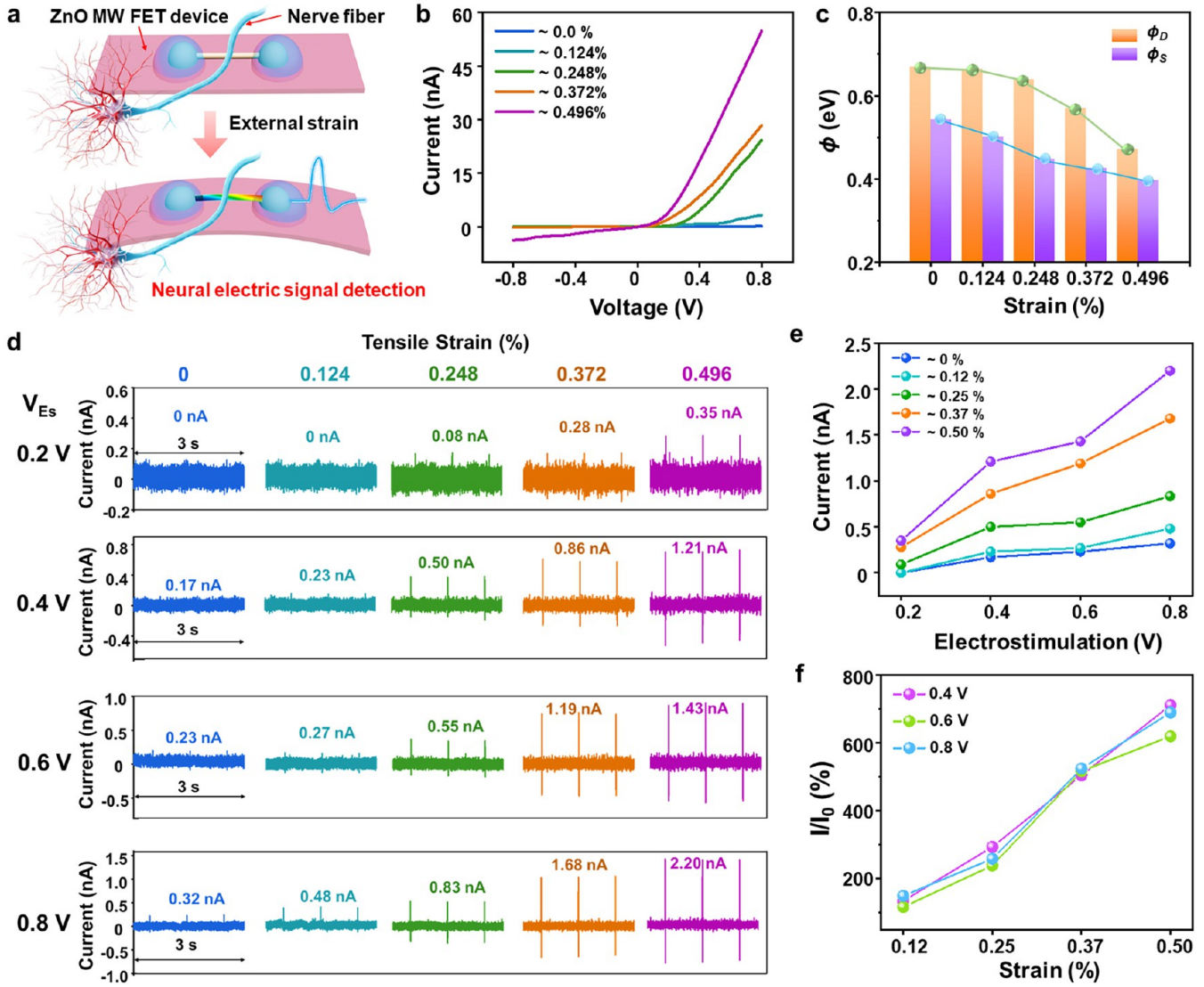

Figure 6. Piezotronic effect enhanced the performance of the ZnO NMW sensor in detecting neural electric impulses. (a) Schematic of a ZnO NMW neural electric impulse sensor under no external strain or tensile strain. (b) *I*−*V* curves of the ZnO NMW sensor at different degrees of tensile strain. (c) SBH of the drain and source as a function of the degree of tensile strain. (d) The resulting neural electrical responses were measured using the ZnO NMW sensor at different degrees of tensile strain after being stimulated with different voltage pulses (0.2, 0.4, 0.6, and 0.8 V). (e) Current spike amplitude as a function of electrostimulation under different degrees of tensile strain. (f) Relative current response of the ZnO NMW sensor as a function of tensile strain under different electrostimulations.

μM, and most *I*−*V* curves shift downward obviously with an increase of DA concentration.

In the initial state (shown in Figure 5b), the *I*−*V* curves corresponding to 0 M and 100 nM almost overlapped, and the *I*−*V* curve corresponding to 10 μM decreased to a limit when the output currents in the range of −1 V to 1 V are near zero. From this *I*−*V* curve, we can see that the lowest and highest DA concentrations that the sensor can detect are higher than 100 nM and lower than 10 μM, respectively. When the tensile strain increased from 0.00 to 0.24 and 0.36%, the *I*−*V* curves corresponding to 0 M and 100 nM were separated, and the *I*−*V* curve corresponding to 10 μM still had the space to decrease. These results indicate that the detection range of DA is greater than 100 nM to 10 μM, and the detection range can be increased by the piezotronic effect.

Figure S8a−d shows the piezotronic effect on the *I*−*V* curves of the DA biosensor at DA concentrations of 0 M, 100 nM, 1, and 10 μM, respectively, and all *I*−*V* curves shift upward with increasing tensile strain. To clearly show the DA sensing performance of the Schottky-contacted ZnO NMW FET device at different DA concentrations and tensile strains, output currents at 1.0 V from Figure 5b−d were organized and plotted in a three-dimensional (3D) graph, as shown in Figure 5e, where the output currents at a bias voltage of 1.0 V increase with the increase of tensile strain or decrease of DA concentration. The current change (ΔI) at different DA concentrations increases with the degree of tensile strain (Figure 5f). In the initial state, the difference between the current at 0 M and that at 100 nM is 1.77 nA, while this difference under tensile strains ∼0.24% and ∼0.36% increases to 16.4 and 25.8 nA, respectively, which is increased by more than 9 and 14 times, respectively, indicating that the piezotronic effect lowered the lowest DA concentration that the DA sensor could detect from 500 to 100 nM.

Moreover, the SBHs at the source calculated from the *I*−*V* curves (0−1 V) of Figure 5b−d were organized and plotted in

https://doi.org/10.1021/acsami.4c21235
ACS Appl. Mater. Interfaces XXXX, XXX, XXX−XXX

a 3D graph, as shown in Figure 5g, where the SBHs of the source increased with increasing DA concentration and decreased with the degree of tensile strain. This is because the negatively charged DA molecules binding on the ZnO surface deplete the electrons in ZnO NMW and increase the conduction and valence bands of ZnO, which leads to an increase of SBH (Figure S9) and can be decreased by the positive piezopotential induced by the tensile strain. The variation in SBH explains the change in the $I-V$ curve with the variation in the tensile strain and DA concentration and also clarifies the improved sensing performance of the fabricated ZnO NMW DA sensor. In addition, ZnO NMW can be coated with 10 nm-thick Al_2O_3 shells by the atomic layer deposition technique to ensure long-term stability if used *in vivo*, which also potentially avoids monoamines generated by ZnO NMW interference with accurate detection.[58]

Besides detecting biomolecules, NW-based FET devices are also widely used to record neural electric impulses. In this section, the effect of external strain on the sensitivity of the Schottky-contacted ZnO NMW FET device to record neural electric signals was studied, and the bullfrog sciatic nerve trunk was selected as the nerve fiber (Figure 6a). For the ZnO NMW FET device, the $I-V$ curve in the range of −0.8 and +0.8 V shifts upward as the tensile strain increases from 0 to 0.496% (Figure 6b), and the SBHs of the source and drain calculated from Figure 6b decrease as the tensile strain increases. The bullfrog sciatic nerve trunk was stimulated by different voltage pulses (0.2, 0.4, 0.6, and 0.8 V; 1 Hz, 0.1 ms), and the traces of electrostimulation voltage pulses are shown in Figure S10. The primary and enlarged output current responses of the ZnO NMW biosensor under different degrees of tensile strains are shown in Figures 6c and S11, respectively.

When the stimulating voltage is 0.2 V, vibrant contraction of the frog gastrocnemius muscle can be observed, which means that the action potential is generated and flows through the ZnO NMW; however, the weak feature signal of the action potential is not detected by the ZnO NMW biosensor under no external strain and tensile strain of 0.124%. When the tensile strain reaches 0.248%, the amplitude of the feature signal is about 0.08 nA, and with an increase of tensile strain, the amplitude of the feature signal increases to 0.35 nA. The piezotronic effect induced by tensile strain improves the ability of the ZnO NMW biosensor to detect weak signals.

To clearly show the variation trend of the current response amplitude to different electrostimulations at different tensile strains, the amplitude of the feature signal and the signal-to-noise ratio summarized and calculated from Figure 6d were plotted in two-dimensional (2D) graphs and 3D graphs, as shown in Figures 6e and S12, and the sensing performance (amplitude of the feature signal and signal-to-noise ratio) increased with the stimulation voltage and degree of tensile strain. The current response amplitude can be significantly enhanced by the tensile strain-induced piezotronic effect. For instance, under a tensile strain of 0.496%, the current response amplitude can be increased by a factor of 6.2−7.1 (Figure 6f). When the neural electric signal is recorded, the ZnO NMW biosensor under tensile strain exhibits a wider detection range and higher intensity than that under no external strain.

This phenomenon is in accordance with the transconductance modulation principle. An action potential is a rapid sequence of voltage changes across a membrane (Figure S13a). When the action potential flows through the ZnO NMW, the varying membrane voltage or potential is equivalent to applying a varying gate voltage (V_G) to the ZnO NMW FET device (Figure S13b). The positive and negative V_G increased or decreased the conduction of ZnO NMW, respectively. According to the conclusions reported in previous works,[24] the performance of NMW FET devices for receiving and amplifying V_G is usually defined as transconductance. The relationship between the extrinsic transconductance (g_{ex}) measured in experiments and the intrinsic transconductance (g_{in}) is

$$g_{ex} = \frac{g_{in}}{1 + g_{in}(R_1 + R_{sh1}) + (R_{sh1} + R_1 + R_2)/R_{wire}}$$

$$\text{or} g_{ex} = \frac{g_{in}}{1 + g_{in}(R_2 + R_{sh2}) + (R_{sh2} + R_2 + R_1)/R_{wire}} \quad (1)$$

where R_{sh1} and R_{sh2} are the shunt resistances associated with the two Schottky barriers, and R_1 and R_2 are the equivalent contact resistances of the Ag electrode and ZnO NMW, respectively, when the SBHs decrease to 0 (Figure S13c). When tensile strain is applied to the ZnO NMW FET sensor, the induced positive piezopotential lowers the SBH at the source and drain, the SBH equivalent resistances R_{Sh1} and R_{Sh2} both decrease, and g_{ex} (representing the sensitivity for recording the neural electric signal) can be improved.

Analysis of the equation and our previous studies revealed that the ohmic-contact nano-FET biosensor exhibited superior performance (higher g_{ex}) compared to the Schottky-contact nano-FET biosensor, whereas the ohmic-contact biosensor demonstrated a lack of sensitivity to biomolecules. Although TENG treatment has been documented to facilitate the reversible conversion between Schottky and Ohmic contacts in FETs, the SBHs reduced by this method are temporally unstable and gradually recover with time.[26] The SBH recovery process, which can extend from tens of minutes to several hours, renders the device unsuitable for monitoring biomolecular concentration fluctuations during this interval. By contrast, the MCPD exhibits stable SBHs under constant piezoelectric deformation/strain, offering the additional benefit of a rapid SBH alteration time frame, measured in seconds. Moreover, the sensitivities of Schottky-contact nano-FET biosensors for detecting biomolecules and neural electric signals can also be simultaneously enhanced by the MF-induced piezoelectric effect, which is of great importance for the future realization of nano-FET-based neural interface devices to achieve highly sensitive detection of both signals simultaneously *in vivo*. For ohmic-contact nano-FET biosensors, the sensing performance for detecting biomolecules and neural electrical signals would not be further enhanced by the piezotronic effect. However, the sensing performance for sensing neural electrical signals could be enhanced by improving the quality of the biointerface between the device and brain tissue realized by MF-induced external strain, which will be explored in detail in the next section.

2.5. Magnetic Actuation of On-Demand Contact between Devices and the Cerebral Cortex. Compared to traditional piezoelectric devices, the distinct advantage of MCPD lies in the realization of remote, precise, and stable piezoelectric deformation through MF actuation. This feature renders the MCPD design suitable for regulating piezoelectric devices implanted *in vivo*. If the MCPD serves as a semi-invasive neural interface device implanted within the human

https://doi.org/10.1021/acsami.4c21235
ACS Appl. Mater. Interfaces XXXX, XXX, XXX−XXX

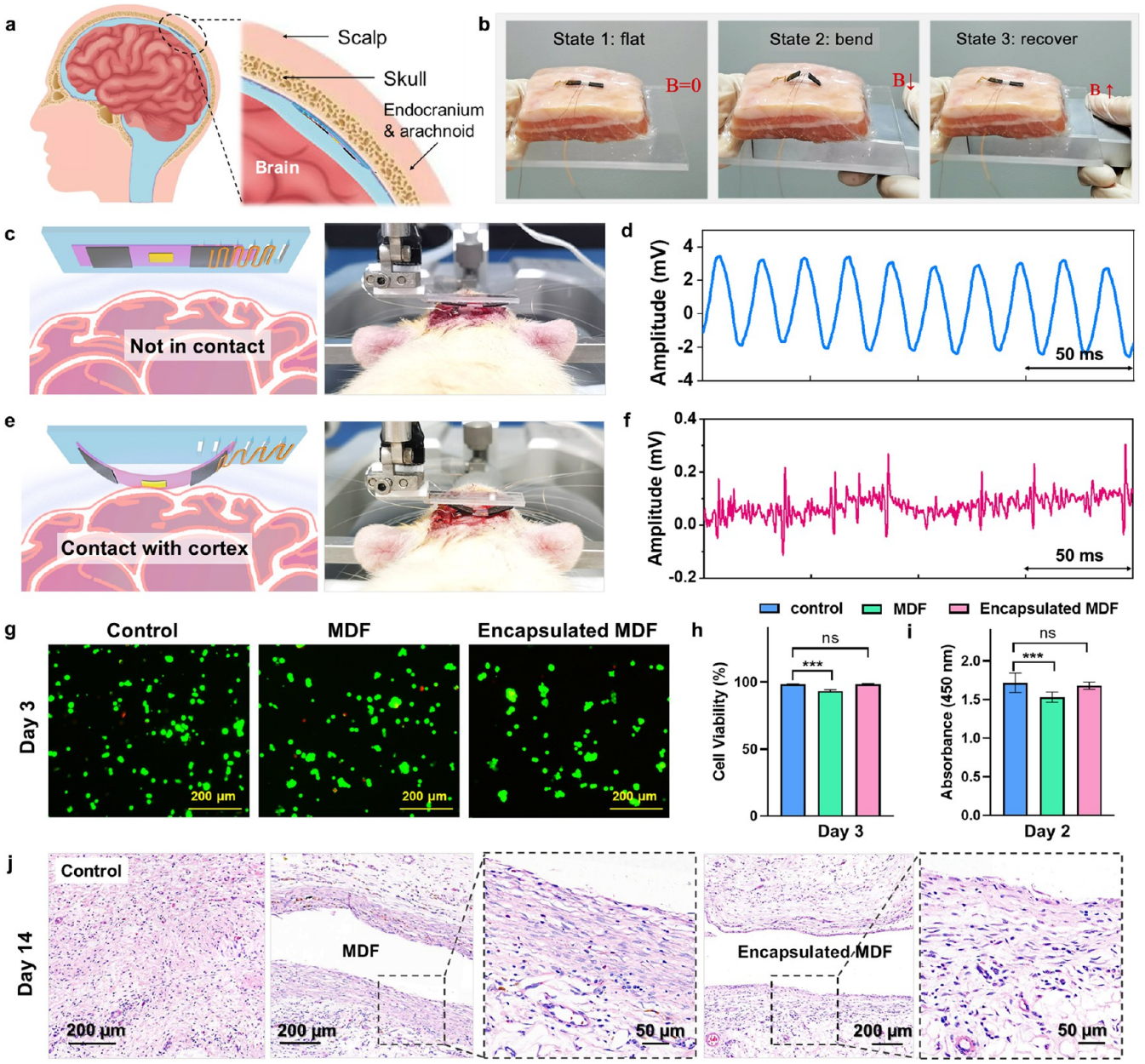

Figure 7. Magnetic actuation of on-demand contact between devices and the cerebral cortex. (a) Schematic diagram of the application scenario of MCPD implantation *in vivo*. (b) MCPD driven by a magnet to transform between the flat state and bend state attenuated by 2 cm-thick pork. (c) Schematic diagram and photograph of the magnetically controllable neural electrode (MCNE) not in contact with the cortex. (d) Traces of signals recorded by electrodes fabricated on the MCNE from the anesthetized rat brain (not in contact). (e) Schematic diagram and photograph of MCNE in contact with the cortex after being driven by MF. (f) Traces of electrophysiological signals recorded by electrodes fabricated on the MCNE from anesthetized rat brain (contact). (g) Live/dead staining results of PC-12 cells in the control group, MDF group, and encapsulated MDF group on day 3. (h) Statistical results for the cell viability of live/dead staining. Error bars in h indicate SD for $n = 3$ measurements. (i) Absorbance of the CCK8 results in the cells of the control group, MDF group, and encapsulated MDF group on day 2. Error bars in i indicate SD for $n = 8$ measurements. (j) Photographs of hematoxylin and eosin (H&E) staining results of the control group, MDF group, and encapsulated MDF group after 14 days.

skull for the detection of neurotransmitter and neural electrical signals, the MF needs to penetrate the scalp, skull, endocranium, and arachnoid membranes (Figure 7a). While it is established that MFs are not attenuated or distorted by biological fluids and tissues, the decay of MF with distance presents a challenge. The scalp and skull thickness typically range from 2 to 3 mm and 1 to 1.5 cm, respectively, with the distance between the endocranium and pia mater of humans being approximately 0.5 cm. In this work, the MCPD was demonstrated to transform between a flat and a bent state under the influence of an MF attenuated by 2 cm of pork tissue, generated by a permanent magnet with a size of 100 × 50 × 20 mm^3 (Figure 7b). The transformation process is described in detail in Movie 2. The induced stable bent state of MCPD not only exerts external strain on piezoelectric biological sensors, which can be used to regulate SBH to enhance sensing performance but also facilitates a high-quality biointerface between the semi-invasive MCPD and brain

https://doi.org/10.1021/acsami.4c21235
ACS Appl. Mater. Interfaces XXXX, XXX, XXX−XXX

tissue, which is crucial for the high-quality recording of electrophysiological signals.

Based on the results in Figure 7b and Movie 3, we intend to verify the feasibility of remotely controlling neural interface devices to make contact with or detach from the cerebral cortex *via* MF actuation. For simplicity, a magnetically controllable neural electrode (MCNE) was prepared by replacing the piezoelectric sensor of the MCPD with a metal neural electrode (Figure S14) and fixed above the head of an SD rat. When the MCNE was in the flat state, the metal electrode did not contact the exposed cortex of the anesthetized rat brain (Figure 7c), resulting in the acquisition of only noise signals (Figure 7d). Upon application of a temporary MF to induce the bending of MCNE, the metal electrode made sufficient contact with the exposed cortex (Figure 7e), enabling the recording of electrophysiological signals from the anesthetized rat brain (Figure 7f). The whole process of MCNE contact with and detachment from the cortex of an SD rat is shown in Movie 3. For semi-invasive neural electrodes positioned on the epidural or subdural surface of the cerebral cortex, the novel MCNE structure offers a new strategy for enhancing the quality of electrophysiological signals during contact. Moreover, the Kapton film of the MCNE is a commonly used substrate for fabricating flexible neural microelectrode arrays, which imbue implantable flexible neural microelectrode arrays with the potential for remote-driven contact with brain tissue during recording and subsequent detachment from the cerebral cortex, retracting to attach the endocranium by the elastic tether after recording. Therefore, magnetic actuation of the on-demand contact between neural electrodes and the cerebral cortex presents a novel and potential strategy to reduce the risk of nerve tissue damage and chronic inflammation stemming from prolonged contact or friction between neural electrodes and the soft cerebral cortex, a concept that warrants further investigation.

For long-term application *in vivo*, the biocompatibility of MCPD was preliminarily evaluated. PDMS and Kapton are widely used materials for constructing intracranial neural interface devices owing to their excellent biocompatibility and biosafety. However, NdFeB particles used in the preparation of MDF have been shown to exhibit biotoxicity. To address this, MDFs were encapsulated in an ultrathin layer of PDMS to enhance biocompatibility. A comprehensive evaluation of both unencapsulated and PDMS-encapsulated MDFs was conducted. Live/dead staining of PC-12 cells revealed significantly lower viability in the MDF group than in the control and encapsulated MDF groups, with no significant difference observed between the latter two groups (Figure 7g,h). The CCK8 results further demonstrated enhanced cell compatibility of the encapsulated MDF (Figure 7i). Histological examination of the subcutaneous tissue after 14 days showed that the PDMS-encapsulated MDF group had fewer inflammatory cell infiltrations and slower fibrous sheath formation around the implants, indicating good biocompatibility (Figure 7j). The findings presented herein demonstrate that MCPD, with its PDMS-encapsulated MDF component, possesses the necessary biocompatibility for *in vivo* applications. Future research should focus on further optimizing MCPD to reduce its size, enhance its sensitivity, and decrease the magnetic field strength required for deformation.

3. CONCLUSIONS

In this study, we proposed a new type of magnetically controllable piezoelectric device that shows the development of films that undergo deformation upon exposure to a MF. We successfully harnessed the piezotronic effect induced by the external strain generated by our MCPD to effectively modulate the SBHs of the ZnO NMW FET devices. To maintain the stable strain of the piezoelectric device after the MF is withdrawn, MCPD with unique structures of grooves, a patch, and an S-shaped elastic tether was presented. This innovative design allows for a reversible transformation between a flat state and various bend states, enabling the flexible tuning and stable maintenance of SBHs in piezoelectric devices. By optimizing the SBHs of ZnO NMW-based biosensors through the piezotronic effect, we significantly enhanced the sensing performance of ZnO NMW-based biosensors for detecting neurobiological signals, such as the concentration of DA molecules and neural electrical signals. Additionally, for *in vivo* applications, we confirmed the feasibility of transcranial MF control of MCPD and demonstrated the biocompatibility of MDF used. The MF-actuated state conversion realizes MCNE contact with or detachment from the brain tissue on demand, thereby enhancing the quality of the biointerface between the neural electrodes and brain tissue for acquiring high-quality electrophysiological signals. In conclusion, this work presents novel concepts for modulating piezoelectric bioelectronics implanted *in vivo* and paves the way for the development of neural interface devices with exceptional sensing performance and biocompatibility, as well as implantable piezoelectric materials that can be remotely activated and suitable for long-term implantation.

4. EXPERIMENTAL SECTION

4.1. Fabrication of Magnetic Composite Films. The magnetic composite film was prepared by homogeneously mixing NdFeB microparticles of different sizes into an uncured PDMS (SYLGARD 184) resin or soft silicone rubber (Ecoflex 00−10) with different mass ratios. The obtained mixture was then cast onto a mold prepared using a 3D printer and placed in an oven at 60 °C. After curing, thin films with different thicknesses were produced. The magnetic composite films were then folded and magnetized by an MF (about 1.0 T) generated by the magneto-optic Kerr effect system (Evico magnetics GmbH/em-Kerr-high res).

4.2. Magnetic and Mechanical Characterization of Magnetic Composite Films. The M−H loops of MDF were measured using a physical property measurement system (PPMS DynaCool). The bending angle of the MDF was defined as the angle between the horizontal line and the upturned end of the MDF under an MF. The strength of the MF generated by the magnet has an attenuation relationship with the increase in distance (Figure S2). The variation in the bending angle of the MDF with the strength of MF was recorded by video, the magnetic field strength was measured by a Gaussmeter, and the bending angle of the MDF was measured by screen capture of the video. To study the effect of the thickness of MDF, the concentration and size of the NdFeB particles, and the mechanical properties of elastomers on the bending angle of the MDF, each group contained 3 MDF for statistical analysis. The stress−strain curves were measured using a universal testing machine (ZQ-990B).

4.3. Fabrication and Performance Characterization of the ZnO NMW-Based Device. The ZnO NMWs used were synthesized by the reported vapor−liquid−solid method.[28] An individual ZnO NMW was transferred to the center location of MDP or the Kapton film, and both ends of the ZnO NMW were fixed using silver paste. When the ZnO NMW-based devices serve as biosensors for detecting DA concentration and neural electric signals, the silver paste should be covered by a thin epoxy layer for waterproofing. The $I-V$ curves of

https://doi.org/10.1021/acsami.4c21235
ACS Appl. Mater. Interfaces XXXX, XXX, XXX−XXX

the ZnO NMW-based device were measured using an electrochemical workstation (ZQ-990B).

4.4. Fabrication of the Magnetically Controllable Piezoelectric Device (MCPD). The ZnO NMW-based FET device was fabricated on a flexible layer of the Kapton film (0.025 mm), and one end of the Kapton film substrate was fixed on the PDMS substrate with grooves by curing the PDMS solution. Two pieces of MDF, a Kapton film patch, and an S-shaped elastic tether made by a laser engraver were assembled according to Figure 4d, and the units were fixed by curing the PDMS solution.

4.5. Surface Functionalization and DA Detection. The ZnO NMW-based device was treated with O_2 plasma for 10 min followed by immersion in 5% (*v*/*v*) APTES in ethanol solution at room temperature for 11 min, and then gently rinsed with ethanol and DI water. After drying, 20 μL of 4-CPBA activated with EDC and NHS in a 1 mM MES buffer solution (4-CPBA/EDC/NHS = 1:1:1) was dropped onto the surface of the ZnO NMW. When the drop completely evaporated at room temperature, the activated device was rinsed with 10 mM MES buffer solution and DI water and dried in air. During the detection of DA, *I*−*V* curves were measured after the DA solutions with different concentrations were dropped onto the device for 5 min.

4.6. Recording of Neural Electric Impulses. This study was approved by the Ethics Committee of Biology and Medicine at Dalian University of Technology (approval number: DUTFM240827-01). After dissecting the bullfrog, the sciatic nerve trunk was immersed in the Ringer's solution for 10 min to maintain activity before stimulation, and it was kept wet by Ringer's solution throughout the experiment. Then, the obtained nerve trunk was aligned across the ZnO NMW-based biosensor. The stimulating voltage impulses (0.2 − 0.8 V, 1 Hz, 0.1 ms) were generated by a signal generator (ArbStudio 1104). The *I*−*t* curves of the ZnO NMW-based biosensor were continuously recorded at a fixed voltage by an electrometer (KEITHLEY 6517B).

4.7. Biocompatibility Test of MDF and Encapsulated MDF. A thin layer of 50 μm-thick PDMS film was spin-coated onto the MDF to serve as a package layer. PC-12 cells were used for cell biocompatibility tests. The cells were seeded and cultured in MDF and encapsulated MDF-leached culture medium and cultured in pristine culture medium as the control group. On day 2, the viability of PC-12 cells was analyzed using the CCK-8 assay (Abcam). 10% CCK-8 solution and 90% culture medium from the control group, MDF group, and encapsulated MDF group were incubated with PC-12 cells for 1 h. The culture medium containing CCK-8 was added to a 96-well plate at 200 μL/well. The absorbance values of the solutions were measured at 450 nm using a microplate absorbance assay instrument (Varioskan Lux, Thermofisher). On day 3, the PC-12 cells were stained with calcein-AM solution (live)/ ethidium homodimer solution (dead) to detect live/dead cells. PC-12 cell staining was observed under a fluorescence microscope (DM6000, Leica).

MDFs and encapsulated MDFs were implanted under the subdermal layer of SD rats to observe the tissue compatibility of the films. After 14 days of implantation, the skin and subcutaneous tissue were collected at the implantation site for HE staining.

4.8. Electrophysiological Recording on the Rat Brain Surface. Anesthesia was induced by a 4% high concentration of isoflurane, and when the SD rat was completely anesthetized, it was immediately transferred to the stereoscope for fixation. The anesthesia concentration was maintained at about 2−2.5%, and the airflow was 500−700 mL/min. The hair between the ear and eyelines at the top of the skull was cut off, and the craniofacial skin was exposed and disinfected with iodophor. Eye glue was applied to the eyes to protect the SD rats from visual damage. Ophthalmic scissors were used to cut the skin at the top of the skull, and a cotton swab dipped in hydrogen peroxide was used to clean the skull surface. A cranial nail was drilled into the posterior fontanel skull to secure the ground. A dental drill was used to drill a window-opening hole into the skull, exposing the right hemisphere with a 5 × 5 mm^2 window opening. Saline drops were added to keep the exposed brains moist. A raised metal neural electrode was formed by soldering tin onto a copper tape with an electric soldering iron. The metal electrode was placed on the middle of the Kapton substrate, and the MCNE was fabricated. The MCNE was fixed above the top of the skull of the SD rats and neural signals were recorded using the Blackrock Microsystems CerePlex Direct when the MCNE was in contact with or detached from the exposed cortex. After data acquisition, the rats were euthanized.

4.9. Animal Experiments. All animal experiments were approved by the Ethics Committee of Biology and Medicine at Dalian University of Technology (approval number: DUTFM240827-01).

■ ASSOCIATED CONTENT

Supporting Information

The Supporting Information is available free of charge at https://pubs.acs.org/doi/10.1021/acsami.4c21235.

Photograph and schematic diagram of MDF magnetization and evaluating process; repeatability of the MCPD device; stability of SBH regulated by the piezotronic effect method; piezotronic effect enhanced the sensing performance of ZnO NMW-based biosensor; traces of nerve fiber electrostimulations with voltage pulses, photograph of MCNE (PDF)

State transition realized by applying MF with a duration of only a few seconds; state transition of MCPD realized by remote control; the whole process of MCNE contact with and detachment from the cortex of an SD rat (ZIP)

■ AUTHOR INFORMATION

Corresponding Authors

Zhou Li − *Beijing Institute of Nanoenergy and Nanosystems, Chinese Academy of Sciences, Beijing 101400, China;* orcid.org/0000-0002-9952-7296; Email: zli@binn.cas.cn

Bo Liu − *Central Hospital of Dalian University of Technology, Dalian 116021 Liaoning, China; Faculty of Medicine, Liaoning Key Lab of Integrated Circuit and Biomedical Electronic System, Dalian University of Technology, Dalian 116024, China;* orcid.org/0000-0002-5375-0505; Email: lbo@dlut.edu.cn

Authors

Luming Zhao − *Central Hospital of Dalian University of Technology, Dalian 116021 Liaoning, China; Beijing Institute of Nanoenergy and Nanosystems, Chinese Academy of Sciences, Beijing 101400, China; Faculty of Medicine, Liaoning Key Lab of Integrated Circuit and Biomedical Electronic System, Dalian University of Technology, Dalian 116024, China*

Hangyu Zhang − *Central Hospital of Dalian University of Technology, Dalian 116021 Liaoning, China; Faculty of Medicine, Liaoning Key Lab of Integrated Circuit and Biomedical Electronic System, Dalian University of Technology, Dalian 116024, China*

Changyong Wang − *Beijing Institute of Basic Medical Sciences, Beijing 100850, China*

Jin Zhou − *Beijing Institute of Basic Medical Sciences, Beijing 100850, China;* orcid.org/0000-0003-3128-407X

Meng Xiao − *Beijing Institute of Nanoenergy and Nanosystems, Chinese Academy of Sciences, Beijing 101400, China*

Jian Cheng − *Beijing Institute of Nanoenergy and Nanosystems, Chinese Academy of Sciences, Beijing 101400, China*

https://doi.org/10.1021/acsami.4c21235
ACS Appl. Mater. Interfaces XXXX, XXX, XXX−XXX

Jing Huang − *Beijing Institute of Nanoenergy and Nanosystems, Chinese Academy of Sciences, Beijing 101400, China*

Lingling Xu − *Beijing Institute of Nanoenergy and Nanosystems, Chinese Academy of Sciences, Beijing 101400, China*

Tianyu Gao − *Central Hospital of Dalian University of Technology, Dalian 116021 Liaoning, China; Faculty of Medicine, Liaoning Key Lab of Integrated Circuit and Biomedical Electronic System, Dalian University of Technology, Dalian 116024, China*

Zunhui Zhao − *Central Hospital of Dalian University of Technology, Dalian 116021 Liaoning, China; Faculty of Medicine, Liaoning Key Lab of Integrated Circuit and Biomedical Electronic System, Dalian University of Technology, Dalian 116024, China*

Complete contact information is available at: https://pubs.acs.org/10.1021/acsami.4c21235

Author Contributions

The manuscript was written through the contributions of all authors. All authors have given approval to the final version of the manuscript.

Notes

The authors declare no competing financial interest.

■ ACKNOWLEDGMENTS

The authors are grateful for the support received from the National Key R&D project of the Ministry of Science and Technology, China (2022YFB3804700-), STI 2030—Major Projects (2021ZD0201600), National Natural Science Foundation of China (No. 32201120 and T2125003), and the Fundamental Research Funds for the Central Universities.

■ REFERENCES

(1) Shi, Q.; Sun, Z.; Le, X.; Xie, J.; Lee, C. Soft Robotic Perception System with Ultrasonic Auto-Positioning and Multimodal Sensory Intelligence. *ACS Nano* **2023**, *17* (5), 4985−4998.

(2) Chen, G.; Fang, Y.; Zhao, X.; Tat, T.; Chen, J. Textiles for learning tactile interactions. *Nat. Electron.* **2021**, *4* (3), 175−176.

(3) Li, T.; Yuan, Y.; Gu, L.; Li, J.; Shao, Y.; Yan, S.; Zhao, Y.; Carlos, C.; Dong, Y.; Qian, H.; Wang, X.; Wu, W.; Wang, S.; Wang, Z.; Wang, X. Ultrastable piezoelectric biomaterial nanofibers and fabrics as an implantable and conformal electromechanical sensor patch. *Sci. Adv.* **2024**, *10* (29), No. eadn8706.

(4) Hinchet, R.; Yoon, H. -J.; Ryu, H.; Kim, M. -K.; Choi, E. -K.; Kim, D. -S.; Kim, S. -W. Transcutaneous ultrasound energy harvesting using capacitive triboelectric technology. *Science* **2019**, *365* (6452), 491−494.

(5) Chung, Y.; Jeong, J. -M.; Hwang, J. -H.; Kim, Y. -J.; Park, B. -J.; Cho, D. S.; Cho, Y.; Suh, S. -J.; Choi, B. -O.; Park, H. -M.; Yoon, H. -J.; Kim, S. -W. Gigantic triboelectric power generation overcoming acoustic energy barrier using metal-liquid coupling. *Joule* **2024**, *8* (9), 2681−2695.

(6) Zhang, Z.; Zhu, Z.; Zhou, P.; Zou, Y.; Yang, J.; Haick, H.; Wang, Y. Soft Bioelectronics for Therapeutics. *ACS Nano* **2023**, *17* (18), 17634−17667.

(7) Cea, C.; Zhao, Z.; Wisniewski, D. J.; Spyropoulos, G. D.; Polyravas, A.; Gelinas, J. N.; Khodagholy, D. Integrated internal ion-gated organic electrochemical transistors for stand-alone conformable bioelectronics. *Nat. Mater.* **2023**, *22* (10), 1227−1235.

(8) Zhang, A.; Lee, J. -H.; Lieber, C. M. Nanowire-enabled bioelectronics. *Nano Today* **2021**, *38*, No. 101135.

(9) Zhang, A.; Lieber, C. M. Nano-Bioelectronics. *Chem. Rev.* **2016**, *116* (1), 215−257.

(10) Lee, D. -M.; Kang, M.; Hyun, I.; Park, B. -J.; Kim, H. J.; Nam, S. H.; Yoon, H. -J.; Ryu, H.; Park, H. -m.; Choi, B. -O.; Kim, S. -W. An on-demand bioresorbable neurostimulator. *Nat. Commun.* **2023**, *14* (1), No. 7315.

(11) Lim, C.; Park, C.; Sunwoo, S. -H.; Kim, Y. G.; Lee, S.; Han, S. I.; Kim, D.; Kim, J. H.; Kim, D. -H.; Hyeon, T. Facile and Scalable Synthesis of Whiskered Gold Nanosheets for Stretchable, Conductive, and Biocompatible Nanocomposites. *ACS Nano* **2022**, *16* (7), 10431−10442.

(12) Zhao, Y.; You, S. S.; Zhang, A.; Lee, J. -H.; Huang, J.; Lieber, C. M. Scalable ultrasmall three-dimensional nanowire transistor probes for intracellular recording. *Nat. Nanotechnol.* **2019**, *14* (8), 783−790.

(13) Ledesma, H. A.; Li, X.; Carvalho-de-Souza, J. L.; Wei, W.; Bezanilla, F.; Tian, B. An atlas of nano-enabled neural interfaces. *Nat. Nanotechnol.* **2019**, *14* (7), 645−657.

(14) Shi, D.; Narayanan, S.; Woeppel, K.; Cui, X. T. Improving the Biocompatibility and Functionality of Neural Interface Devices with Silica Nanoparticles. *Acc. Chem. Res.* **2024**, *57* (12), 1684−1695.

(15) Chen, L.; Wen, C.; Zhang, S. -L.; Wang, Z. L.; Zhang, Z. -B. Artificial tactile peripheral nervous system supported by self-powered transducers. *Nano Energy* **2021**, *82*, No. 105680.

(16) Han, S. I.; Sunwoo, S. -H.; Park, C. S.; Lee, S. -P.; Hyeon, T.; Kim, D. -H. Next-Generation Cardiac Interfacing Technologies Using Nanomaterial-Based Soft Bioelectronics. *ACS Nano* **2024**, *18* (19), 12025−12048.

(17) Patolsky, F.; Timko, B. P.; Yu, G.; Fang, Y.; Greytak, A. B.; Zheng, G.; Lieber, C. M. Detection, Stimulation, and Inhibition of Neuronal Signals with High-Density Nanowire Transistor Arrays. *Science* **2006**, *313* (5790), 1100−1104.

(18) Shi, J.; Sun, C.; Liang, E.; Tian, B. Semiconductor Nanowire-Based Cellular and Subcellular Interfaces. *Adv. Funct. Mater.* **2022**, *32* (11), No. 2107997.

(19) Tian, B.; Lieber, C. M. Nanowired Bioelectric Interfaces. *Chem. Rev.* **2019**, *119* (15), 9136−9152.

(20) Wei, T. -Y.; Yeh, P. -H.; Lu, S. -Y.; Wang, Z. L. Gigantic Enhancement in Sensitivity Using Schottky Contacted Nanowire Nanosensor. *J. Am. Chem. Soc.* **2009**, *131* (48), 17690−17695.

(21) Hu, Y.; Zhou, J.; Yeh, P. -H.; Li, Z.; Wei, T. -Y.; Wang, Z. L. Supersensitive, Fast-Response Nanowire Sensors by Using Schottky Contacts. *Adv. Mater.* **2010**, *22* (30), 3327−3332.

(22) Meng, J.; Li, Z. Schottky-Contacted Nanowire Sensors. *Adv. Mater.* **2020**, *32* (28), No. 2000130.

(23) Zhou, J.; Gu, Y.; Hu, Y.; Mai, W.; Yeh, P. -H.; Bao, G.; Sood, A. K.; Polla, D. L.; Wang, Z. L. Gigantic enhancement in response and reset time of ZnO UV nanosensor by utilizing Schottky contact and surface functionalization. *Appl. Phys. Lett.* **2009**, *94* (19), No. 191103.

(24) Niu, S.; Hu, Y.; Wen, X.; Zhou, Y.; Zhang, F.; Lin, L.; Wang, S.; Wang, Z. L. Enhanced Performance of Flexible ZnO Nanowire Based Room-Temperature Oxygen Sensors by Piezotronic Effect. *Adv. Mater.* **2013**, *25* (27), 3701−3706.

(25) Yeh, P. -H.; Li, Z.; Wang, Z. L. Schottky-Gated Probe-Free ZnO Nanowire Biosensor. *Adv. Mater.* **2009**, *21* (48), 4975−4978.

(26) Zhao, L.; Li, H.; Meng, J.; Wang, A. C.; Tan, P.; Zou, Y.; Yuan, Z.; Lu, J.; Pan, C.; Fan, Y.; Zhang, Y.; Zhang, Y.; Wang, Z. L.; Li, Z. Reversible Conversion between Schottky and Ohmic Contacts for Highly Sensitive, Multifunctional Biosensors. *Adv. Funct. Mater.* **2020**, *30* (5), No. 1907999.

(27) Hu, Y.; Chang, Y.; Fei, P.; Snyder, R. L.; Wang, Z. L. Designing the Electric Transport Characteristics of ZnO Micro/Nanowire Devices by Coupling Piezoelectric and Photoexcitation Effects. *ACS Nano* **2010**, *4* (2), 1234−1240.

(28) Xue, F.; Zhang, L.; Feng, X.; Hu, G.; Fan, F. R.; Wen, X.; Zheng, L.; Wang, Z. L. Influence of external electric field on piezotronic effect in ZnO nanowires. *Nano Res.* **2015**, *8* (7), 2390−2399.

(29) Pan, C.; Zhai, J.; Wang, Z. L. Piezotronics and Piezo-phototronics of Third Generation Semiconductor Nanowires. *Chem. Rev.* **2019**, *119* (15), 9303−9359.

(30) Zhou, J.; Gu, Y.; Fei, P.; Mai, W.; Gao, Y.; Yang, R.; Bao, G.; Wang, Z. L. Flexible Piezotronic Strain Sensor. *Nano Lett.* **2008**, *8* (9), 3035−3040.
(31) Zhao, L.; Li, H.; Meng, J.; Zhang, Y.; Feng, H.; Wu, Y.; Li, Z. Combining triboelectric nanogenerator with piezoelectric effect for optimizing Schottky barrier height modulation. *Sci. Bull.* **2021**, *66* (14), 1409−1418.
(32) Li, H.; Zhao, L.; Meng, J.; Pan, C.; Zhang, Y.; Zhang, Y.; Liu, Z.; Zou, Y.; Fan, Y.; Wang, Z. L.; Li, Z. Triboelectric-polarization-enhanced high sensitive ZnO UV sensor. *Nano Today* **2020**, *33*, No. 100873.
(33) Yu, R.; Niu, S.; Pan, C.; Wang, Z. L. Piezotronic effect enhanced performance of Schottky-contacted optical, gas, chemical and biological nanosensors. *Nano Energy* **2015**, *14*, 312−339.
(34) Guo, J.; Wen, R.; Liu, Y.; Zhang, K.; Kou, J.; Zhai, J.; Wang, Z. L. Piezotronic Effect Enhanced Flexible Humidity Sensing of Monolayer MoS_2. *ACS Appl. Mater. Interfaces* **2018**, *10* (9), 8110−8116.
(35) Cao, X.; Cao, X.; Guo, H.; Li, T.; Jie, Y.; Wang, N.; Wang, Z. L. Piezotronic Effect Enhanced Label-Free Detection of DNA Using a Schottky-Contacted ZnO Nanowire Biosensor. *ACS Nano* **2016**, *10* (8), 8038−8044.
(36) Chen, C.; Yu, Q.; Liu, S.; Qin, Y. Piezotronic Transistors Based on GaN Wafer for Highly Sensitive Pressure Sensing with High Linearity and High Stability. *ACS Nano* **2024**, *18* (21), 13607−13617.
(37) Yu, Q.; Ge, R.; Wen, J.; Du, T.; Zhai, J.; Liu, S.; Wang, L.; Qin, Y. Highly sensitive strain sensors based on piezotronic tunneling junction. *Nat. Commun.* **2022**, *13* (1), No. 778.
(38) Eichenfield, M.; Michael, C. P.; Perahia, R.; Painter, O. Actuation of micro-optomechanical systems via cavity-enhanced optical dipole forces. *Nat. Photonics* **2007**, *1* (7), 416−422.
(39) Luo, X.; Mather, P. T. Conductive shape memory nanocomposites for high speed electrical actuation. *Soft Matter* **2010**, *6* (10), 2146−2149.
(40) Moulton, T.; Ananthasuresh, G. K. Micromechanical devices with embedded electro-thermal-compliant actuation. *Sens. Actuators, A* **2001**, *90* (1), 38−48.
(41) Ren, Z.; Hu, W.; Dong, X.; Sitti, M. Multi-functional soft-bodied jellyfish-like swimming. *Nat. Commun.* **2019**, *10* (1), No. 2703.
(42) Zhao, X.; Zhou, Y.; Li, A.; Xu, J.; Karjagi, S.; Hahm, E.; Rulloda, L.; Li, J.; Hollister, J.; Kavehpour, P.; Chen, J. A self-filtering liquid acoustic sensor for voice recognition. *Nat. Electron.* **2024**, *7* (10), 924−932.
(43) Liu, Y.; Chen, X.; Liang, Y.; Song, H.; Yu, P.; Guan, S.; Liu, Z.; Yang, A.; Tang, M.; Zhou, Y.; Zheng, Y.; Yang, Z.; Jiang, L.; He, J.; Tan, N.; Xu, B.; Lin, X. Ferromagnetic Flexible Electronics for Brain-Wide Selective Neural Recording. *Adv. Mater.* **2023**, *35* (6), No. 2208251.
(44) Dong, Y.; Wang, L.; Xia, N.; Yang, Z.; Zhang, C.; Pan, C.; Jin, D.; Zhang, J.; Majidi, C.; Zhang, L. Untethered small-scale magnetic soft robot with programmable magnetization and integrated multifunctional modules. *Sci. Adv.* **2022**, *8* (25), No. eabn8932.
(45) Wang, C.; Wu, Y.; Dong, X.; Armacki, M.; Sitti, M. In situ sensing physiological properties of biological tissues using wireless miniature soft robots. *Sci. Adv.* **2023**, *9* (23), No. eadg3988.
(46) Hou, Y.; Wang, H.; Fu, R.; Wang, X.; Yu, J.; Zhang, S.; Huang, Q.; Sun, Y.; Fukuda, T. A review on microrobots driven by optical and magnetic fields. *Lab Chip* **2023**, *23* (5), 848−868.
(47) Coles, L.; Ventrella, D.; Carnicer-Lombarte, A.; Elmi, A.; Troughton, J. G.; Mariello, M.; El Hadwe, S.; Woodington, B. J.; Bacci, M. L.; Malliaras, G. G.; Barone, D. G.; Proctor, C. M. Origami-inspired soft fluidic actuation for minimally invasive large-area electrocorticography. *Nat. Commun.* **2024**, *15* (1), No. 6290.
(48) Jiang, Y.; Tian, B. Inorganic semiconductor biointerfaces. *Nat. Rev. Mater.* **2018**, *3* (12), 473−490.
(49) Gao, L.; Wang, J.; Guan, S.; Du, M.; Wu, K.; Xu, K.; Zou, L.; Tian, H.; Fang, Y. Magnetic Actuation of Flexible Microelectrode Arrays for Neural Activity Recordings. *Nano Lett.* **2019**, *19* (11), 8032−8039.
(50) Chi, M.; Zhao, Y.; Zhang, X.; Jia, M.; Yu, A.; Wang, Z. L.; Zhai, J. A Piezotronic and Magnetic Dual-Gated Ferroelectric Semiconductor Transistor. *Adv. Funct. Mater.* **2023**, *33* (46), No. 2307901.
(51) Liu, W.; Lee, M.; Ding, L.; Liu, J.; Wang, Z. L. Piezopotential Gated Nanowire−Nanotube Hybrid Field-Effect Transistor. *Nano Lett.* **2010**, *10* (8), 3084−3089.
(52) Wang, Z. L. Piezopotential gated nanowire devices: Piezotronics and piezo-phototronics. *Nano Today* **2010**, *5* (6), 540−552.
(53) Zhang, Y.; Hu, Y.; Xiang, S.; Wang, Z. L. Effects of piezopotential spatial distribution on local contact dictated transport property of ZnO micro/nanowires. *Appl. Phys. Lett.* **2010**, *97* (3), No. 033509.
(54) Ryspayeva, A.; Jones, T. D. A.; Esfahani, M. N.; Shuttleworth, M. P.; Harris, R. A.; Kay, R. W.; Desmulliez, M. P. Y.; Marques-Hueso, J. A rapid technique for the direct metallization of PDMS substrates for flexible and stretchable electronics applications. *Microelectron. Eng.* **2019**, *209*, 35−40.
(55) Goldstein, D. S.; Holmes, C.; Sharabi, Y. Cerebrospinal fluid biomarkers of central catecholamine deficiency in Parkinson's disease and other synucleinopathies. *Brain* **2012**, *135* (6), 1900−1913.
(56) Hyun, T. -H.; Cho, W. -J. High-Performance FET-Based Dopamine-Sensitive Biosensor Platform Based on SOI Substrate. *Biosensors* **2023**, *13* (5), No. 516.
(57) Lin, C. -H.; Hsiao, C. -Y.; Hung, C. -H.; Lo, Y. -R.; Lee, C. -C.; Su, C. -J.; Lin, H. -C.; Ko, F. -H.; Huang, T. -Y.; Yang, Y. -S. Ultrasensitive detection of dopamine using a polysilicon nanowire field-effect transistor. *Chem. Commun.* **2008**, No. 44, 5749−5751.
(58) Zhou, W.; Dai, X.; Fu, T. -M.; Xie, C.; Liu, J.; Lieber, C. M. Long Term Stability of Nanowire Nanoelectronics in Physiological Environments. *Nano Lett.* **2014**, *14* (3), 1614−1619.

https://doi.org/10.1021/acsami.4c21235
ACS Appl. Mater. Interfaces XXXX, XXX, XXX−XXX